



RESEARCH ARTICLE

[View Article Online](#)
[View Journal](#) | [View Issue](#)

 Cite this: *Inorg. Chem. Front.*, 2023, **10**, 1818

Electrochemical conversion of CO₂ into HCOO[−] in a synergistic manner by a nanocomposite of Zn₂SnO₄/ZnO†

 Yingzheng Zhang,^a Zijian Li,^b Haeseong Jang,^{c,d} Xiaoqian Wei,^a Qing Qin ^{*a} and Xien Liu ^{*a}

Exploring environmentally friendly nanomaterials as alternatives to toxic metals for electrocatalytic CO₂ reduction into formate is very important. Designing a nanocomposite catalyst with different phase components is an underlying strategy to achieve prominent catalysts for electrochemical CO₂ reduction owing to the potential capacity to regulate electronic structure by interfacial interactions. Herein, we report a novel nanocomposite with components of cubic-like Zn₂SnO₄ and nanosheet-structured ZnO (Zn₂SnO₄/ZnO) as an efficient electrocatalyst for the CO₂ reduction reaction (CO₂RR). This strategy can reduce the use of toxic metals and the cost of the catalyst. The composite exhibited a maximum faradaic efficiency (FE) of 98% for the C₁ product, and even approached 90% for formate production at −1.0 V versus the reversible hydrogen electrode, along with excellent durability. In contrast, the maximum FE_{HCOOH} of a single ZnO component or Zn₂SnO₄ component were both <50% over the potential window. Coupling of X-ray photoelectron/adsorption spectroscopy and electrochemical measurements revealed interfacial charge transfer and oxygen vacancies to result in an optimized electronic structure of Zn₂SnO₄/ZnO. This was favorable for an HCOO* intermediate-involved reaction pathway, together with an enlarged electrochemical active area, which boosted the selectivity and activity of formate synergistically.

 Received 30th December 2022,
 Accepted 9th February 2023

DOI: 10.1039/d2qi02762c

rsc.li/frontiers-inorganic

Introduction

The rapid rising of the carbon dioxide level in the Earth's atmosphere has caused serious climate change and subsequent chain reactions.^{1–5} Methods usually employed for CO₂ conversion include thermal catalysis, photocatalysis, and electrocatalysis. Among these methods, electrocatalytic CO₂ reduction to valuable fuels and chemicals powered by renewable energy resources can alleviate environmental issues effectively, but also realize the recycling of energy, thereby attracting great interest.^{6,7} The products of an electrochemical CO₂ reduction reaction (CO₂RR) are diverse: CO, HCOOH, CH₄, C₂H₅OH, C₂H₄, and C₂H₆.^{8,9} Among them, HCOOH is considered to be a crucial raw material for basic organic chemicals

that is commonly applied in food additives, printing, and dyeing.¹⁰ Formate is a potential choice for storing and delivering liquid hydrogen. Formate can release H₂ if needed, and can be used as a chemical fuel for direct formate fuel cells. Besides, as a liquid product, formate can be stored and transported readily, and saves the cost of liquefaction processes compared with gas products. Thus, formate presents the highest net value and is economically competitive if evaluated from a technoeconomic aspect.¹¹ However, CO₂ electroreduction to formate is hindered due to the high chemical inertness of CO₂ (bond energy = 806 kJ mol^{−1}), so a high overpotential is needed for activation.¹² In addition, CO₂RR involves competition from multiple reaction paths and is usually accompanied by other competitive side reactions, especially the hydrogen-evolution reaction (HER). Even though considerable effort has been devoted to promoting formate production, many problems are encountered, such as a low conversion rate and poor selectivity. Therefore, developing high-performance electrocatalysts to facilitate the CO₂-to-formate conversion is highly desired, but challenging.

Some metals and their oxides electrodes, such as Pb,¹³ Bi,¹⁴ Sn,¹⁵ and In,¹⁶ possess relatively high selectivity towards CO₂ reduction to formate. However, the expense of Pd, as well as the toxicity and environmental unfriendliness of In and Pd,

^aCollege of Chemical Engineering, Qingdao University of Science and Technology, Qingdao 266042, China. E-mail: qinqing@qust.edu.cn, liuxien@qust.edu.cn

^bDepartment of Chemistry, City University of Hong Kong, Hong Kong, China

^cBeamline Research Division, Pohang Accelerator Laboratory (PAL), Pohang 790-784, Korea

^dEnergy Storage and Distributed Resources Division Berkeley, Lawrence Berkeley National Laboratory, California 94720, USA

 †Electronic supplementary information (ESI) available. See DOI: <https://doi.org/10.1039/d2qi02762c>

makes them unsuitable for large-scale application. Hence, catalysts composed of elements characterized by high abundance and nontoxicity have garnered more attention. Recently, zinc-based catalysts have aroused wide interest due to the low cost, nontoxicity, and capacity for electrocatalytic CO₂ reduction.^{17–19} For example, a ZnO sheet array supported on Zn foil showed a high faradaic efficiency (FE) of 85% for CO₂RR to CO at –2.0 V (vs. Ag/AgCl).²⁰ Moreover, Ce_{0.016}Zn_{0.984}O exhibited a maximum FE_{CO} of 88% at –1.0 V vs. the reversible hydrogen electrode (RHE) and excellent stability for continuous testing.²¹ Hence, Zn-based catalysts tend to electrocatalyze the reduction of CO₂ to CO. Can the selectivity of ZnO be changed from CO to formate by dual engineering of electronic structure and morphology? In general, the precise manipulation of a component, morphology and size is an effective method to regulate the energy efficiency and selectivity for CO₂RR by the “electronic effect” and “geometric effect”.²²

Creation of heterostructures with different components affords a feasible approach for engineering the CO₂RR performance by “tuning” the electronic structure.^{12,23} Due to a strong interaction at the interface, CuO/In₂O₃ composites enable remarkable electroreduction activity of CO₂ to CO with a FE_{CO} of 93.0% at –0.7 vs. RHE.²⁴ Guan and co-workers²⁵ reported that SnO₂/ZnO composites exhibited enhanced performance of CO₂-to-HCOO[–] conversion with a maximum FE_{HCOO[–]} of 76.70% at –1.16 V vs. RHE. Interfacial charge transport is enhanced in Zn₂SnO₄/SnO₂ heterostructures, which greatly reduces the kinetic barriers of CO₂RR and results in excellent selectivity for HCOOH.¹² In addition, nanostructuring of composite catalysts would create preferential faceting, vacancy defects and more unsaturated coordination sites, thereby tuning their electronic structure as well as the binding energy of key intermediates.²⁶

Herein, we developed an effective strategy for promoting CO₂ electroreduction to formate by constructing a nanocomposite catalyst with Zn₂SnO₄ and ZnO phase components. With low Sn content of 6.65 wt%, the resultant Zn₂SnO₄/ZnO composite catalyst with oxygen vacancies exhibited greatly enhanced activity and selectivity for electrochemical CO₂ reduction to formate, with a maximum FE_{HCOOH} of 87% at –1.0 V vs. RHE and a larger partial current density of formate (46 mA cm^{–2}), which was markedly superior to those of a single ZnO component or Zn₂SnO₄ component. Based on experimental analyses, the improved catalytic performance could be ascribed to three aspects. The first was a cubic-like structured Zn₂SnO₄ and nanosheet-structured ZnO that enabled intimate contact with each other, providing abundant ZnO-Zn₂SnO₄ heterostructure interfaces, promoting charge redistribution and altering the electronic structure. Second, the nanostructured hybrids were beneficial for mass transport and enlarged the contact between reaction intermediates and the Zn₂SnO₄/ZnO catalyst. Third, the optimized electronic properties were in favour of a HCOO* intermediate-involved reaction pathway (Fig. S1†), and thereby enhanced the selectivity of formate. This work highlights the design of composite electrocatalysts to render excellent catalytic performance by intimate interface interaction.

Results and discussion

A facile one-step hydrothermal method was applied to prepare the Zn₂SnO₄/ZnO composite catalyst. As displayed by the X-ray diffraction (XRD) pattern in Fig. 1a, all the peaks closely matched the main characteristic peaks of hexagonal-phase ZnO with a *P63mc*(186) space group (JCPDS number: 36-1451)²⁷ and cubic-phase Zn₂SnO₄ (JCPDS number: 24-1470).²⁸ Compared with pristine ZnO, the diffraction peaks of ZnO in Zn₂SnO₄/ZnO composite showed a slight shift towards a high diffraction angle (Fig. S2†), thereby demonstrating the strong interaction between ZnO and Zn₂SnO₄. This interaction may result in compressive strain in a composite catalyst and be favourable for reducing the energy barrier of HCOOH production, especially the potential-limiting step.²⁹ The scanning electron microscope (SEM) image of the Zn₂SnO₄/ZnO catalyst is shown in Fig. 1b. It demonstrates the coexistence of a nanosheet and nano-cube in Zn₂SnO₄/ZnO, which was further confirmed by the transmission electron microscopy (TEM) image in Fig. 1c. As evidenced by a high-angle annular dark field (HAADF)-STEM image and corresponding elemental mappings in Fig. 1f–i, the component in Zn₂SnO₄/ZnO with nanosheet morphology was ZnO, whereas Zn₂SnO₄ was cubic. The thickness of the ZnO nanosheet was ~20 nm, and resulted in more exposed active sites and increased the carrier density of the catalyst.³⁰ Furthermore, the ZnO in Zn₂SnO₄/ZnO composite had a rough surface with many pore structures, which greatly improved the mass transfer rate of the catalyst (Fig. S3†). Fig. 1d shows the high-resolution TEM (HRTEM) image of the ZnO constituent. The clear lattice fringes with interlayer spacings of 0.16 nm and 0.26 nm were assigned to the (100) and (002) planes of ZnO, respectively. The inset of Fig. 1d shows the corresponding FFT image, which distinctly shows a single-crystal structure with excellent crystallinity. The HRTEM image and corresponding FFT pattern of the Zn₂SnO₄ constituent are displayed in Fig. 1e. The clear lattice spacing of 0.26 nm was assigned to the (311) planes of Zn₂SnO₄ with a *Fd* $\bar{3}$ *m* space group. Inductively coupled plasma-optical emission spectrometry (ICP-OES) revealed a relatively low Sn content of ~6.65 wt% in the composite. Evidently, the Zn₂SnO₄/ZnO composite had been synthesized successfully. To show the great advantage of forming a composite for electrochemical CO₂ reduction, pristine ZnO and Zn₂SnO₄ were also prepared by a one-step hydrothermal method. The XRD patterns in Fig. S4 and S5† demonstrate the phases of the prepared reference materials to be hexagonal-phase ZnO and cubic-phase Zn₂SnO₄. Fig. S6† shows the SEM image of synthesized ZnO. Accordingly, the ZnO catalyst exhibited a nanosheet morphology with a similar thickness to that in the Zn₂SnO₄/ZnO composite, which increased the number of exposed active sites for CO₂RR.

To gain deep insight into the coordination environment and electronic state of the Zn₂SnO₄/ZnO catalyst, X-ray photoelectron spectroscopy (XPS), X-ray absorption near-edge structure spectroscopy (XANES), and extended X-ray absorption fine structure (EXAFS) spectroscopy were carried out. The XPS survey spectrum in Fig. 2a shows the constituent elements of



Fig. 1 (a) XRD pattern of $\text{Zn}_2\text{SnO}_4/\text{ZnO}$. (b) SEM image of $\text{Zn}_2\text{SnO}_4/\text{ZnO}$. (c) TEM image of $\text{Zn}_2\text{SnO}_4/\text{ZnO}$. (d) HRTEM image and corresponding FFT pattern of the ZnO constituent. (e) HRTEM image and corresponding FFT pattern of the Zn_2SnO_4 constituent. (f) STEM of $\text{Zn}_2\text{SnO}_4/\text{ZnO}$. (g–i) EDS mapping of Zn, O and Sn.

Zn, Sn, and O in $\text{Zn}_2\text{SnO}_4/\text{ZnO}$, which was in agreement with the elemental mapping results stated above. The Zn 2p spectrum of ZnO exhibited two symmetrical peaks of Zn $2p_{3/2}$ and Zn $2p_{1/2}$ at 1020.6 and 1043.8 eV, respectively (Fig. 2b).³¹ The two peaks corresponding to Zn $2p_{3/2}$ and $2p_{1/2}$ of Zn_2SnO_4 were located at 1022.8 eV and 1045.9 eV. The two relative peaks in $\text{Zn}_2\text{SnO}_4/\text{ZnO}$ were positioned at 1021.19 and 1044.28 eV, respectively. These results demonstrated that the valence of Zn in the $\text{Zn}_2\text{SnO}_4/\text{ZnO}$ composite had been optimized, and lay between that of pristine Zn_2SnO_4 and ZnO, and perhaps contributed to the enhanced activity and selectivity towards CO_2 electroreduction to formate. Fig. 2c shows the Sn 3d XPS spectra of $\text{Zn}_2\text{SnO}_4/\text{ZnO}$ and Zn_2SnO_4 . In the case of Zn_2SnO_4 , the two main peaks with binding energies of 494.2 eV and 485.6 eV belonged to the Sn $3d_{3/2}$ and Sn $3d_{5/2}$ of Sn^{4+} .³² Two smaller peaks at 492.5 eV and 484.0 eV were ascribed to the small amount of metallic Sn.³³ When forming a composite with ZnO, both of these two peaks of Sn $3d_{3/2}$ and Sn $3d_{5/2}$ of

Sn^{4+} showed a slight shift towards high binding energies and were located at 494.7 and 486.1 eV, respectively, thereby indicating electron depletion around Sn atoms.³² In the high-resolution O 1s spectrum of Zn_2SnO_4 , two peaks centered at 529.3 eV and 530.5 eV were attributed to the coordination of O in Sn–O–Sn and Sn–O–Zn, respectively (Fig. 2d).¹² For ZnO, two peaks with binding energies of 529.9 and 531.3 eV could be observed in the O 1s spectrum, and were attributed to lattice O and oxygen vacancies (O_v).³⁴ When forming $\text{Zn}_2\text{SnO}_4/\text{ZnO}$ composite materials, the peaks related to O_v and lattice O shifted to high binding energies, which demonstrated the charge redistribution in a composite system. These O_v defects play an important part in increasing the selectivity of formate and the active sites of CO_2RR .^{35,36} Furthermore, the H^* adsorption free energy could be weakened by O_v and, thus, inhibit the HER side reaction.^{37–39}

Fig. 3a displays the Zn K-edge XANES spectrum of $\text{Zn}_2\text{SnO}_4/\text{ZnO}$ compared with prepared ZnO, commercial ZnO (Comm.

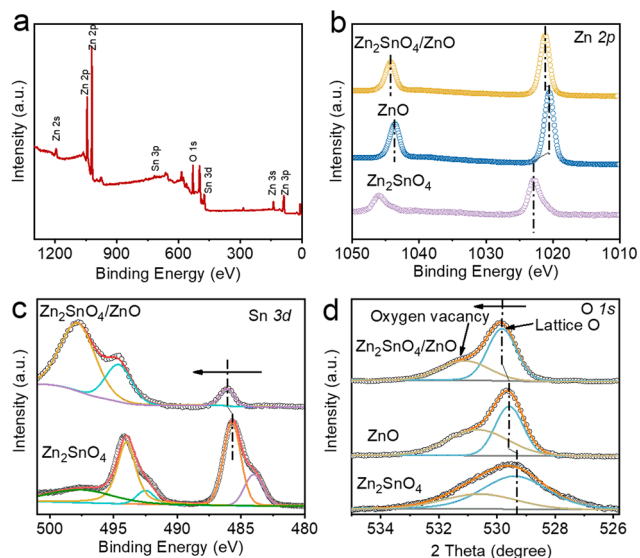


Fig. 2 Characterizations of electronic structure. (a) XPS survey spectrum of $\text{Zn}_2\text{SnO}_4/\text{ZnO}$. (b) High-resolution Zn 2p XPS spectra of $\text{Zn}_2\text{SnO}_4/\text{ZnO}$, ZnO and Zn_2SnO_4 . (c) High-resolution Sn 3d XPS spectra of $\text{Zn}_2\text{SnO}_4/\text{ZnO}$ and Zn_2SnO_4 . (d) High-resolution O 1s XPS spectra of $\text{Zn}_2\text{SnO}_4/\text{ZnO}$, ZnO and Zn_2SnO_4 .

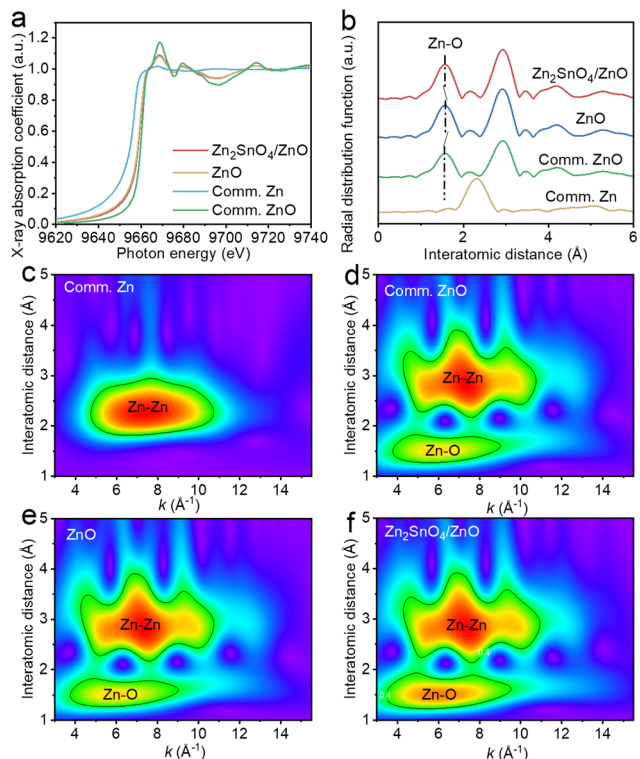


Fig. 3 (a) Zn K-edge XANES and (b) k^3 -weighted FT-EXAFS spectra of ZnO, $\text{Zn}_2\text{SnO}_4/\text{ZnO}$ and reference materials. WT analysis of (c) Comm. Zn, (d) Comm. ZnO, (e) ZnO and (f) $\text{Zn}_2\text{SnO}_4/\text{ZnO}$.

ZnO), and commercial Zn (Comm. Zn). In the case of prepared ZnO, the main absorption peak at 9668 eV and anterior resonance peak of 9683 eV are typical features of hexagonal-phase

ZnO.³⁵ However, its pre-edge adsorption exhibited an obvious negative shift in comparison with that of Comm. ZnO, thereby demonstrating the lower oxidation state of Zn in prepared ZnO.³⁶ Meanwhile, the pre-edge adsorption of $\text{Zn}_2\text{SnO}_4/\text{ZnO}$ had a slightly positive shift compared with that of prepared ZnO, but lower than that of Comm. ZnO, implying that the valence state of Zn in formed $\text{Zn}_2\text{SnO}_4/\text{ZnO}$ was lower than +2. The Fourier transform (FT) spectra of $\text{Zn}_2\text{SnO}_4/\text{ZnO}$ and reference samples are shown in Fig. 3b. The first coordination shell in prepared ZnO had Zn–O coordination with a scattering peak at 1.58 Å, which was right-shifted by 0.02 Å compared with that in Comm. ZnO, and demonstrated an elongated Zn–O bond in prepared ZnO compared with that in Comm. ZnO. However, the peak associated with Zn–O coordination was located at 1.57 Å for $\text{Zn}_2\text{SnO}_4/\text{ZnO}$. This value was larger than that of Comm. ZnO but smaller than that of prepared ZnO, which indicated the charge redistribution of the $\text{Zn}_2\text{SnO}_4/\text{ZnO}$ composite. To further study the changes in valence state and electronic structure, R and k space-involved wavelet transform (WT) analyses were undertaken. The WT EXAFS contour plots of Comm. ZnO, Comm. Zn, prepared ZnO and $\text{Zn}_2\text{SnO}_4/\text{ZnO}$ are shown in Fig. 3c–f. The WT plots of $\text{Zn}_2\text{SnO}_4/\text{ZnO}$ showed two maxima at 6.27 \AA^{-1} and 7.38 \AA^{-1} , which belonged to Zn–O and Zn–Zn co-ordinations, respectively. The intensity and k -value of the two backscattering paths were similar to those of Comm. ZnO and prepared ZnO, implying the same structural order.

The Sn K-edge XANES spectra of $\text{Zn}_2\text{SnO}_4/\text{ZnO}$ and commercial references are displayed in Fig. 4a. The higher maximum adsorption of $\text{Zn}_2\text{SnO}_4/\text{ZnO}$ than that of commercial SnO_2 (Comm. SnO_2) demonstrated the higher degree of structural distortion.⁴⁰ Moreover, the slightly right-shifted white-line peak of $\text{Zn}_2\text{SnO}_4/\text{ZnO}$ compared with Comm. SnO_2 demonstrated the lower electron density of Sn in the composite. Fig. 4b illustrates the FT-EXAFS spectra of $\text{Zn}_2\text{SnO}_4/\text{ZnO}$, Comm. SnO_2 , Sn and SnO. For Comm. SnO_2 , two scattering peaks related to Sn–O and Sn–Sn were detected. The spectrum of $\text{Zn}_2\text{SnO}_4/\text{ZnO}$ displayed a dominant peak at 1.59 Å (attributed to a Sn–O interaction) and a lower-intensity peak at 3.43 Å (corresponding to a Sn–Sn interaction). Both peaks were negative-shifted relative to those of Comm. SnO_2 . Besides, a new peak appeared at 2.69 Å for $\text{Zn}_2\text{SnO}_4/\text{ZnO}$, which could be assigned to a Sn–Zn interaction.⁴¹ A maximum at 6.6 \AA^{-1} was observed in the WT plots of $\text{Zn}_2\text{SnO}_4/\text{ZnO}$, which corresponded to the Sn–O interaction compared with the references Comm. SnO_2 , SnO and Sn foil (Fig. 4c–f). The k -value of the Sn–O path in $\text{Zn}_2\text{SnO}_4/\text{ZnO}$ was similar to that of Comm. SnO_2 , but the intensity was greater.

The CO_2RR performance of $\text{Zn}_2\text{SnO}_4/\text{ZnO}$ composite was investigated in a flow cell using a three electrode system (Fig. S7†). The performance of pristine Zn_2SnO_4 and ZnO was also evaluated as references. The linear sweep voltammetry (LSV) curves of $\text{Zn}_2\text{SnO}_4/\text{ZnO}$, ZnO and Zn_2SnO_4 in CO_2 -saturated and Ar-saturated 0.5 M KHCO_3 electrolyte are displayed in Fig. S8.† All three catalysts exhibited enhanced current density in the CO_2 -saturated electrolyte than in the Ar-satu-

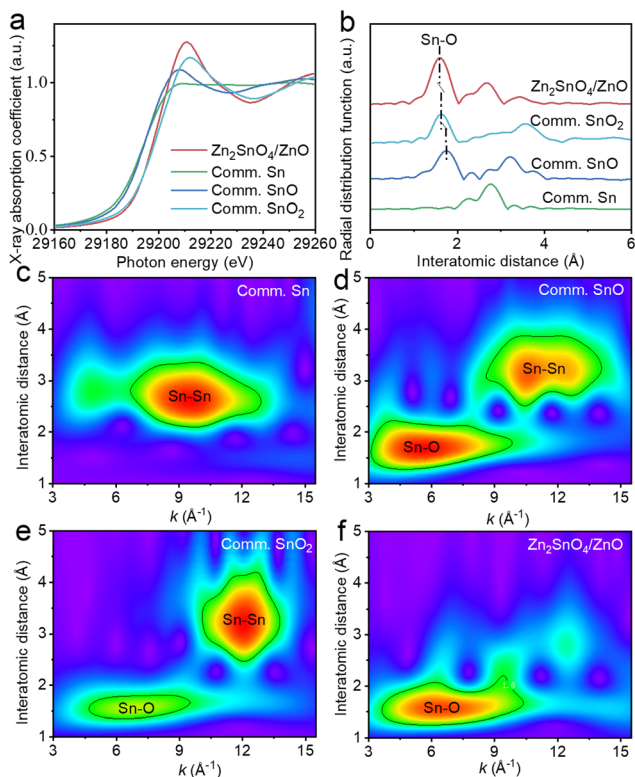


Fig. 4 (a) Sn K-edge XANES and (b) k^3 -weighted FT-EXAFS spectra of $\text{Zn}_2\text{SnO}_4/\text{ZnO}$ and reference materials. WT analysis of (c) Comm. Sn, (d) Comm. SnO, (e) Comm. SnO_2 and (f) $\text{Zn}_2\text{SnO}_4/\text{ZnO}$.

rated electrolyte. More importantly, the current density of $\text{Zn}_2\text{SnO}_4/\text{ZnO}$ in CO_2 -saturated solution was greater than that of pristine ZnO and Zn_2SnO_4 (Fig. 5a), which demonstrated the enhanced activity of a composite catalyst towards CO_2 reduction. The products of CO_2RR on $\text{Zn}_2\text{SnO}_4/\text{ZnO}$ and reference catalysts were evaluated after continuous electrochemical measurement for 1 h under different potentials (Fig. 5b). Gas products were quantified *via* on-line gas chromatography (Fig. S9[†]). Liquid products were measured by ^1H nuclear magnetic resonance (NMR) spectroscopy (Fig. S10[†]). Fig. 5c shows that synthetic ZnO exhibited selectivity for formate production with a maximum faradaic efficiency (FE) of 38% at an applied potential of -0.9 V *vs.* RHE, which is high selectivity for a ZnO -based catalyst for HCOOH production compared with that reported previously. This result could be attributed to oxygen vacancies enhancing CO_2 adsorption and two-dimensional nanosheet morphology, which leads to special crystal orientation. Even so, CO was the main product of CO_2RR on a ZnO catalyst with FE >60% at all applied potentials. In the case of Zn_2SnO_4 , the main product of CO_2RR was HCOOH , but FE_{HCOOH} was <50% over all applied potentials (Fig. 5d). The FE_{CO} and FE_{H_2} for Zn_2SnO_4 are displayed in Fig. S11[†]. Upon formation of a composite, $\text{Zn}_2\text{SnO}_4/\text{ZnO}$ exhibited greatly enhanced selectivity for formate with a maximum FE_{HCOOH} of 87% at -1.0 V *vs.* RHE. Moreover, the FE_{HCOOH} of $\text{Zn}_2\text{SnO}_4/\text{ZnO}$ was maintained at >80% at a wide potential window (-0.8

V to -1.1 V *vs.* RHE) (Fig. 5e and f). The total C_1 products, including CO and formate, was >97% for $\text{Zn}_2\text{SnO}_4/\text{ZnO}$ over a potential window of -0.8 V to -1.1 V *vs.* RHE (Fig. S11[†]), thereby demonstrating a strong capacity for suppressing the HER.

$\text{Zn}_2\text{SnO}_4/\text{ZnO}$ exhibited excellent performance towards HCOOH production in comparison with single ZnO and Zn_2SnO_4 , which corroborated the advantages of a synergistic effect in $\text{Zn}_2\text{SnO}_4/\text{ZnO}$. The partial current density of HCOOH was 46 mA cm^{-2} at -1.1 V *vs.* RHE, which was 2.3-fold and 3.8-fold larger than that of Zn_2SnO_4 and ZnO , respectively (Fig. 5g). The partial current density of H_2 and CO on three typical electrocatalysts is shown in Fig. S12[†]. Accordingly, the half-cell PCE³⁷ of CO_2 -to-formate on the $\text{Zn}_2\text{SnO}_4/\text{ZnO}$ composite was $\sim 45\%$ over the potential window, which was much higher than that of Zn_2SnO_4 and ZnO (Fig. 5h). As illustrated by Fig. 5i, a high formate production rate³⁶ of 0.17 $\mu\text{mol s}^{-1} \text{cm}^{-1}$ was delivered by $\text{Zn}_2\text{SnO}_4/\text{ZnO}$ at -1.1 V *vs.* RHE, which was much higher than that of ZnO (0.08 $\mu\text{mol s}^{-1} \text{cm}^{-1}$) and Zn_2SnO_4 (0.12 $\mu\text{mol s}^{-1} \text{cm}^{-1}$). These data demonstrated the enhanced activity and selectivity of the $\text{Zn}_2\text{SnO}_4/\text{ZnO}$ composite towards CO_2 -to-formate conversion.

Inspired by the superior catalytic performance of the composite electrode, the electrochemical active surface area (ECSA) was measured by cyclic voltammetry under various potentials to assess the number of active sites (Fig. S13[†]). As reported,^{40,42,43} ECSA is directly proportional to double-layer capacitance (C_{dl}). As confirmed by Fig. 6a, $\text{Zn}_2\text{SnO}_4/\text{ZnO}$ exhibited a higher C_{dl} (0.246 mF cm^{-2}) than that of Zn_2SnO_4 (0.162 mF cm^{-2}) or ZnO (0.196 mF cm^{-2}), which indicated more exposed active sites of the composite catalyst. The ECSA of $\text{Zn}_2\text{SnO}_4/\text{ZnO}$, ZnO and Zn_2SnO_4 was calculated to be 0.6 cm^2 , 0.47 cm^2 , and 0.39 cm^2 , respectively. However, the ECSA-normalized partial current density of formate for $\text{Zn}_2\text{SnO}_4/\text{ZnO}$ was 77 mA cm^{-2} at -1.1 V *vs.* RHE, which was 1.5-times and 1.8-times higher than that of Zn_2SnO_4 and ZnO (Fig. 6b), which demonstrated the enhanced intrinsic catalytic activity of active sites in the $\text{Zn}_2\text{SnO}_4/\text{ZnO}$ composite. The enhanced ECSA-normalized total current density also confirmed the improvement of catalytic activity of $\text{Zn}_2\text{SnO}_4/\text{ZnO}$ (Fig. S14[†]). Electrochemical impedance spectroscopy of three typical catalysts were also measured for the study of charge-transfer kinetics (Fig. 6c). $\text{Zn}_2\text{SnO}_4/\text{ZnO}$ possessed the fastest electrode kinetics, as evidenced by the smallest charge transfer resistance (R_{ct}) derived from Nyquist plots.⁴⁴⁻⁴⁶ A chronoamperometric ($i-t$) test at -1.0 V (*vs.* RHE) was conducted to investigate the electrochemical durability of $\text{Zn}_2\text{SnO}_4/\text{ZnO}$. As evidenced by Fig. 6d, $\text{Zn}_2\text{SnO}_4/\text{ZnO}$ could exhibit an increase in total current density during the first hour of testing, which was attributed to activation of the catalyst. Afterwards, a stable total current density of -125 mA cm^{-2} was maintained over 11 h. The FE_{HCOOH} of $\text{Zn}_2\text{SnO}_4/\text{ZnO}$ was >80% over the whole period of stability testing, thereby indicating the excellent electrochemical stability of $\text{Zn}_2\text{SnO}_4/\text{ZnO}$ for CO_2 -to-formate conversion. Accordingly, the greater number of exposed active sites, excellent ability for electron transfer and optimized

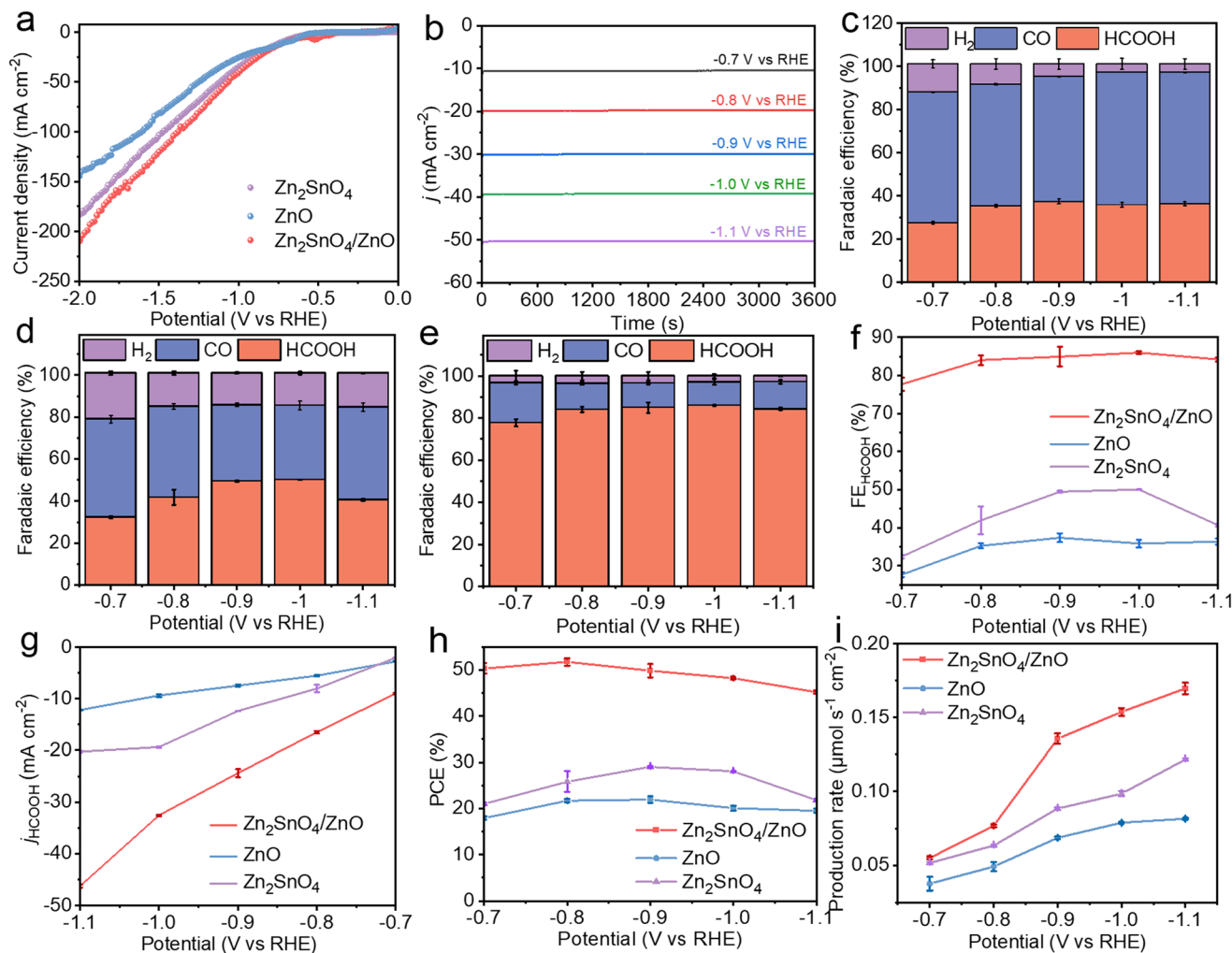


Fig. 5 (a) LSV curves of $\text{Zn}_2\text{SnO}_4/\text{ZnO}$, Zn_2SnO_4 and ZnO in 0.5 M KHCO_3 saturated with CO_2 . (b) $I-t$ curves of $\text{Zn}_2\text{SnO}_4/\text{ZnO}$ at various potentials. FE towards H_2 , CO and HCOOH of (c) prepared ZnO , (d) Zn_2SnO_4 and (e) $\text{Zn}_2\text{SnO}_4/\text{ZnO}$. (f) FE_{HCOOH} of prepared ZnO , Zn_2SnO_4 and $\text{Zn}_2\text{SnO}_4/\text{ZnO}$. (g) HCOOH partial current density of prepared ZnO , Zn_2SnO_4 and $\text{Zn}_2\text{SnO}_4/\text{ZnO}$. (h) Half-cell PCE for CO_2 -to-formate conversion for $\text{Zn}_2\text{SnO}_4/\text{ZnO}$, prepared ZnO and Zn_2SnO_4 , respectively. (i) Formate production rate at different voltages for $\text{Zn}_2\text{SnO}_4/\text{ZnO}$, prepared ZnO and Zn_2SnO_4 .

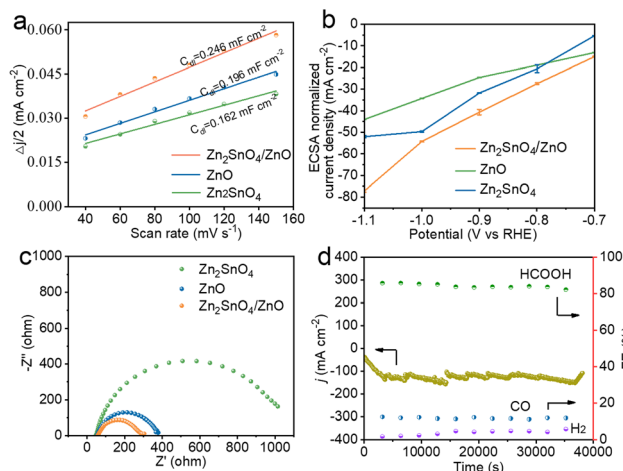


Fig. 6 (a) C_{dl} of $\text{Zn}_2\text{SnO}_4/\text{ZnO}$, Zn_2SnO_4 and ZnO . (b) ECSA-normalized formate partial current density of $\text{Zn}_2\text{SnO}_4/\text{ZnO}$, Zn_2SnO_4 and ZnO . (c) Nyquist plots of $\text{Zn}_2\text{SnO}_4/\text{ZnO}$, Zn_2SnO_4 and ZnO . (d) Stability test on the $\text{Zn}_2\text{SnO}_4/\text{ZnO}$ electrode at -1.0 V (vs. RHE).

surface electronic structure contributed synergistically to the enhanced activity and selectivity of the $\text{Zn}_2\text{SnO}_4/\text{ZnO}$ composite for electroreduction of CO_2 to HCOO^- .

Conclusions

A novel $\text{Zn}_2\text{SnO}_4/\text{ZnO}$ heterostructure nanocomposite catalyst was synthesized *via* a simple one-step hydrothermal method and applied for CO_2 electroreduction in 0.5 M KHCO_3 solution. We report, for the first time, that this $\text{Zn}_2\text{SnO}_4/\text{ZnO}$ hybrid material was employed for electrochemical CO_2 -to-formate conversion. Advanced characterization involving XPS and X-ray adsorption spectroscopy demonstrated the charge redistribution of $\text{Zn}_2\text{SnO}_4/\text{ZnO}$ driven by intimate interfacial interaction. The resultant $\text{Zn}_2\text{SnO}_4/\text{ZnO}$ composite catalyst exhibited significantly enhanced selectivity and activity for CO_2 RR to formate compared with that of constituent ZnO and Zn_2SnO_4 . A remarkable FE_{HCOOH} of up to 87% at -1.0 V vs. RHE was

achieved, surpassing the maximum FE_{HCOOH} of ZnO (38%) and Zn_2SnO_4 (50%) significantly. The greatly enhanced performance for electrochemical CO_2 reduction to formate was due to the optimized electronic structure, higher electrochemically active surface area and the presence of oxygen vacancies on the surface. Our study may provide new insights for the design of electrocatalysts with high selectivity and activity for CO_2RR by a synergistic effect of the constructed nanocomposite.

Conflicts of interest

There are no conflicts to declare.

Acknowledgements

This work was supported by the Taishan Scholar Program of Shandong Province, China (ts201712045), National Natural Science Foundation of China (22102079) and Natural Science Foundation of Shandong Province of China (ZR2021YQ10).

References

- 1 M. Yamamoto-Kawai, F. A. McLaughlin, E. C. Carmack, S. Nishino and K. J. S. Shimada, Aragonite Undersaturation in the Arctic Ocean: Effects of Ocean Acidification and Sea Ice Melt, *Science*, 2009, **326**, 1098–1100.
- 2 X. Duan, J. Xu, Z. Wei, J. Ma, S. Guo, S. Wang, H. Liu and S. Dou, Metal-Free Carbon Materials for CO_2 Electrochemical Reduction, *Adv. Mater.*, 2017, **29**, 1701784.
- 3 M. Zhong, K. Tran, Y. Min, C. Wang, Z. Wang, C.-T. Dinh, P. De Luna, Z. Yu, A. S. Rasouli and P. J. N. Brodersen, Accelerated discovery of CO_2 electrocatalysts using active machine learning, *Nature*, 2020, **581**, 178–183.
- 4 S. C. Peter, Reduction of CO_2 to Chemicals and Fuels: A Solution to Global Warming and Energy Crisis, *ACS Energy Lett.*, 2018, **3**, 1557–1561.
- 5 C.-T. A. Lee, H. Jiang, R. Dasgupta and M. Torres, A Framework for Understanding Whole-Earth Carbon Cycling, *Deep Carbon: Past to Present*, Cambridge University Press, 2019, 313–357.
- 6 S. Zhu, E. P. Delmo, T. Li, X. Qin, J. Tian, L. Zhang and M. Shao, Recent Advances in Catalyst Structure and Composition Engineering Strategies for Regulating CO_2 Electrochemical Reduction, *Adv. Mater.*, 2021, **33**, 2005484.
- 7 J. Feng, S. Zeng, J. Feng, H. Dong and X. J. Zhang, CO_2 Electroreduction in Ionic Liquids: A Review, *Chin. J. Chem.*, 2018, **36**, 961–970.
- 8 Y. Wang, Z. Chen, P. Han, Y. Du, Z. Gu, X. Xu and G. Zheng, Single-Atomic Cu with Multiple Oxygen Vacancies on Ceria for Electrocatalytic CO_2 Reduction to CH_4 , *ACS Catal.*, 2018, **8**, 7113–7119.
- 9 Y. Guo, X. He, Y. Su, Y. Dai, M. Xie, S. Yang, J. Chen, K. Wang, D. Zhou and C. Wang, Machine-Learning-Guided Discovery and Optimization of Additives in Preparing Cu Catalysts for CO_2 Reduction, *J. Am. Chem. Soc.*, 2021, **143**, 5755–5762.
- 10 H. Zeidan and M. E. Marti, Separation of Formic Acid from Aqueous Solutions onto Anion Exchange Resins: Equilibrium, Kinetic, and Thermodynamic Data, *J. Chem. Eng.*, 2019, **64**, 2718–2727.
- 11 I. Dutta, S. Chatterjee, H. Cheng, R. K. Parsapur, Z. Liu, Z. Li, E. Ye, H. Kawanami, J. S. C. Low, Z. Lai, X. J. Loh and K. W. Huang, Formic Acid to Power towards Low-Carbon Economy, *Adv. Energy Mater.*, 2022, **12**, 2103799.
- 12 K. Wang, D. Liu, P. Deng, L. Liu, S. Lu, Z. Sun, Y. Ma, Y. Wang, M. Li, B. Y. Xia, C. Xiao and S. Ding, Band alignment in $\text{Zn}_2\text{SnO}_4/\text{SnO}_2$ heterostructure enabling efficient CO_2 electrochemical reduction, *Nano Energy*, 2019, **64**, 103954.
- 13 W. Zhang, Y. Hu, L. Ma, G. Zhu, Y. Wang, X. Xue, R. Chen, S. Yang and Z. Jin, Progress and Perspective of Electrocatalytic CO_2 Reduction for Renewable Carbonaceous Fuels and Chemicals, *Adv. Sci.*, 2018, **5**, 1700275.
- 14 X. Feng, H. Zou, R. Zheng, W. Wei, R. Wang, W. Zou, G. Lim, J. Hong, L. Duan and H. Chen, $\text{Bi}_2\text{O}_3/\text{BiO}_2$ Nanoheterojunction for Highly Efficient Electrocatalytic CO_2 Reduction to Formate, *Nano Lett.*, 2022, **22**, 1656–1664.
- 15 F. Cheng, X. Zhang, K. Mu, X. Ma, M. Jiao, Z. Wang, P. Limpachanangkul, B. Chalermssinnsuwan, Y. Gao, Y. Li, Z. Chen and L. Liu, Recent Progress of Sn-Based Derivative Catalysts for Electrochemical Reduction of CO_2 , *Energy Technol.*, 2020, **9**, 2000799.
- 16 Y. Huang, X. Mao, G. Yuan, D. Zhang, B. Pan, J. Deng, Y. Shi, N. Han, C. Li, L. Zhang, L. Wang, L. He, Y. Li and Y. Li, Size-Dependent Selectivity of Electrochemical CO_2 Reduction on Converted In_2O_3 Nanocrystals, *Angew. Chem., Int. Ed.*, 2021, **60**, 15844–15848.
- 17 B. Ren, Z. Zhang, G. Wen, X. Zhang, M. Xu, Y. Weng, Y. Nie, H. Dou, Y. Jiang, Y. P. Deng, G. Sun, D. Luo, L. Shui, X. Wang, M. Feng, A. Yu and Z. Chen, Dual-Scale Integration Design of Sn–ZnO Catalyst toward Efficient and Stable CO_2 Electroreduction, *Adv. Mater.*, 2022, **34**, 2204637.
- 18 Z. Zhang, G. Wen, D. Luo, B. Ren, Y. Zhu, R. Gao, H. Dou, G. Sun, M. Feng, Z. Bai, A. Yu and Z. Chen, “Two Ships in a Bottle” Design for Zn–Ag–O Catalyst Enabling Selective and Long-Lasting CO_2 Electroreduction, *J. Am. Chem. Soc.*, 2021, **143**, 6855–6864.
- 19 X. Jiang, F. Cai, D. Gao, J. Dong, S. Miao, G. Wang and X. Bao, Electrocatalytic reduction of carbon dioxide over reduced nanoporous zinc oxide, *Electrochem. Commun.*, 2016, **68**, 67–70.
- 20 H.-i. Nam, K. R. Park, Y.-W. Choi, H.-j. Sim, K. Y. Sohn and D.-H. Lim, Electrocatalytic CO_2 reduction using self-supported zinc sulfide arrays for selective CO production, *Appl. Surf. Sci.*, 2023, **612**, 155646.
- 21 X. Ren, Y. Gao, L. Zheng, Z. Wang, P. Wang, Z. Zheng, Y. Liu, H. Cheng, Y. Dai and B. Huang, Oxygen vacancy enhancing CO_2 electrochemical reduction to CO on Ce-doped ZnO catalysts, *Surf. Interfaces*, 2021, **23**, 100923.

- 22 D. Yang, B. Ni and X. Wang, Heterogeneous Catalysts with Well-Defined Active Metal Sites toward CO₂ Electrocatalytic Reduction, *Adv. Energy Mater.*, 2022, 2001142.
- 23 C. Lv, C. Yan, G. Chen, Y. Ding, J. Sun, Y. Zhou and G. Yu, An Amorphous Noble-Metal-Free Electrocatalyst that Enables Nitrogen Fixation under Ambient Conditions, *Angew. Chem.*, 2018, **130**, 6181–6184.
- 24 S. Chu, S. Hong, J. Masa, X. Li and Z. Sun, Synergistic catalysis of CuO/In₂O₃ composites for highly selective electrochemical CO₂ reduction to CO, *Chem. Commun.*, 2019, **55**, 12380–12383.
- 25 Y. Guan, Y. Liu, J. Yi and J. Zhang, Zeolitic imidazolate framework-derived composites with SnO₂ and ZnO phase components for electrocatalytic carbon dioxide reduction, *Dalton Trans.*, 2022, **51**, 7274–7283.
- 26 L. Wang, W. Chen, D. Zhang, Y. Du, R. Amal, S. Qiao, J. Wu and Z. Yin, Surface strategies for catalytic CO₂ reduction: from two-dimensional materials to nanoclusters to single atoms, *Chem. Soc. Rev.*, 2019, **48**, 5310–5349.
- 27 Z. Zheng, W. Liang, R. Lin, Z. Hu, Y. Wang, H. Lu, W. Zhong, S. Shen and Y. Pan, Facile Synthesis of Zinc Indium Oxide Nanofibers Distributed with Low Content of Silver for Superior Antibacterial Activity, *Small Struct.*, 2023, 2200291.
- 28 Q. Lu, Z. Wei, C. Li, J. Ma and L. Li, Photocatalytic degradation of methyl orange by noble metal Ag modified semiconductor Zn₂SnO₄, *Mater. Sci. Semicond. Process.*, 2022, **138**, 106290.
- 29 Y. Xing, X. Kong, X. Guo, Y. Liu, Q. Li, Y. Zhang, Y. Sheng, X. Yang, Z. Geng and J. Zeng, Bi@Sn Core-Shell Structure with Compressive Strain Boosts the Electroreduction of CO₂ into Formic Acid, *Adv. Sci.*, 2020, **7**, 1902989.
- 30 X. Wan, X. Liu, Y. Li, R. Yu, L. Zheng, W. Yan, H. Wang, M. Xu and J. Shui, Fe–N–C electrocatalyst with dense active sites and efficient mass transport for high-performance proton exchange membrane fuel cells, *Nat. Catal.*, 2019, **2**, 259–268.
- 31 J. Zhang, S. Shao, D. Zhou, Q. Xu and T. Wang, ZnO nanowire arrays decorated 3D N-doped reduced graphene oxide nanotube framework for enhanced photocatalytic CO₂ reduction performance, *J. CO₂ Util.*, 2021, **50**, 101584.
- 32 S. Jain, S. Verma, S. P. Singh and S. N. Sharma, An electrochemical biosensor based on novel butylamine capped CZTS nanoparticles immobilized by uricase for uric acid detection, *Biosens. Bioelectron.*, 2019, **1279**, 135–141.
- 33 Y. Zhang, H. Jang, X. Ge, W. Zhang, Z. Li, L. Hou, L. Zhai, X. Wei, Z. Wang, M. G. Kim, S. Liu, Q. Qin and X. Liu, Single-Atom Sn on Tensile-Strained ZnO Nanosheets for Highly Efficient Conversion of CO₂ into Formate, *Adv. Energy Mater.*, 2022, **12**, 2202695.
- 34 Z. Chen, T. Fan, Y.-Q. Zhang, J. Xiao, M. Gao, N. Duan, J. Zhang, J. Li, Q. Liu, X. Yi and J.-L. Luo, Wavy SnO₂ catalyzed simultaneous reinforcement of carbon dioxide adsorption and activation towards electrochemical conversion of CO₂ to HCOOH, *Appl. Catal., B*, 2020, **261**, 118243.
- 35 R. Daiyan, E. C. Lovell, B. Huang, M. Zubair, J. Leverett, Q. Zhang, S. Lim, J. Horlyck, J. Tang and X. Lu, Uncovering Atomic-Scale Stability and Reactivity in Engineered Zinc Oxide Electrocatalysts for Controllable Syngas Production, *Adv. Energy Mater.*, 2020, **10**, 2001381.
- 36 Z. Geng, X. Kong, W. Chen, H. Su, Y. Liu, F. Cai, G. Wang and J. Zeng, Oxygen Vacancies in ZnO Nanosheets Enhance CO₂ Electrochemical Reduction to CO, *Angew. Chem., Int. Ed.*, 2018, **57**, 6054–6059.
- 37 B. Ning, M. Liu, Y. Hu, H. Jiang and C. Li, Defect engineered SnO₂ nanoparticles enable strong CO₂ chemisorption toward efficient electroconversion to formate, *Dalton Trans.*, 2022, **51**, 3512–3519.
- 38 Y. Ding, L. Zhao, Y. Tong, W. Kong, B. Li, J. Wang, X. Han, W. Xing and J. Xu, Designing High-Performance Se-Decorated Edges of MoSe₂ Nanostripes for the Hydrogen Oxidation Reaction: Effect of Transition Metal Doping, *J. Phys. Chem. C*, 2022, **126**, 13617–13628.
- 39 Z. Li, A. Cao, Q. Zheng, Y. Fu, T. Wang, K. T. Arul, J. L. Chen, B. Yang, N. M. Adli, L. Lei, C. L. Dong, J. Xiao, G. Wu and Y. Hou, Elucidation of the Synergistic Effect of Dopants and Vacancies on Promoted Selectivity for CO₂ Electroreduction to Formate, *Adv. Mater.*, 2021, **33**, 2005113.
- 40 G. Li, H. Jang, S. Liu, Z. Li, M. G. Kim, Q. Qin, X. Liu and J. Cho, The synergistic effect of Hf–O–Ru bonds and oxygen vacancies in Ru/HfO₂ for enhanced hydrogen evolution, *Nat. Commun.*, 2022, **13**, 1270.
- 41 N.-E. Sung, K. H. Chae and I.-J. Lee, Structural Characterization of Zinc-Tin-Oxide Films Deposited on Quartz Substrates by Radio Frequency Magnetron Sputtering, *J. Nanosci. Nanotechnol.*, 2016, **16**, 10356–10360.
- 42 S. Zhou, H. Jang, Q. Qin, L. Hou, M. G. Kim, S. Liu, X. Liu and J. Cho, Boosting Hydrogen Evolution Reaction by Phase Engineering and Phosphorus Doping on Ru/P-TiO₂, *Angew. Chem., Int. Ed.*, 2022, **61**, e202212196.
- 43 X. Jiang, H. Jang, S. Liu, Z. Li, M. G. Kim, C. Li, Q. Qin, X. Liu and J. Cho, The Heterostructure of Ru₂P/WO₃/NPC Synergistically Promotes H₂O Dissociation for Improved Hydrogen Evolution, *Angew. Chem.*, 2021, **133**, 4156–4162.
- 44 S. Ma, J. Deng, Y. Xu, W. Tao, X. Wang, Z. Lin, Q. Zhang, L. Gu and W. Zhong, Pollen-like self-supported FeIr alloy for improved hydrogen evolution reaction in acid electrolyte, *J. Energy Chem.*, 2022, **66**, 560–565.
- 45 S. Shen, Z. Hu, H. Zhang, K. Song, Z. Wang, Z. Lin, Q. Zhang, L. Gu and W. Zhong, Highly Active Si Sites Enabled by Negative Valent Ru for Electrocatalytic Hydrogen Evolution in LaRuSi, *Angew. Chem., Int. Ed.*, 2022, **61**, e202206460.
- 46 Z. Lin, B. Xiao, M. Huang, L. Yan, Z. Wang, Y. Huang, S. Shen, Q. Zhang, L. Gu and W. Zhong, Realizing Negatively Charged Metal Atoms through Controllable d-Electron Transfer in Ternary Ir_{1-x}Rh_xSb Intermetallic Alloy for Hydrogen Evolution Reaction, *Adv. Energy Mater.*, 2022, **12**, 2200855.